Quantitative measurement of the charge carrier concentration using dielectric force microscopy

Junqi Lai(赖君奇)[1,2], Bowen Chen(陈博文)[1,2], Zhiwei Xing(邢志伟)[3], Xuefei Li(李雪飞)[3], Shulong Lu(陆书龙)[2,3], Qi Chen(陈琪)[1,2,†], and Liwei Chen(陈立桅)[1,4,‡]

[1] *i-Lab, CAS Center for Excellence in Nanoscience, Suzhou Institute of Nano-Tech and Nano-Bionics, Chinese Academy of Sciences, Suzhou* 215123, *China*
[2] *School of Nano-Tech and Nano-Bionics, University of Science and Technology of China, Hefei* 230026, *China*
[3] *Key Laboratory of Nanodevices and Applications, Suzhou Institute of Nano-Tech and Nano-Bionics, Chinese Academy of Sciences, Suzhou* 215123, *China*
[4] *In-situ Center for Physical Sciences, School of Chemistry and Chemical Engineering, Shanghai Jiao Tong University, Shanghai* 200240, *China*

(Received 25 July 2022; revised manuscript received 27 November 2022; accepted manuscript online 2 December 2022)

The charge carrier concentration profile is a critical factor that determines semiconducting material properties and device performance. Dielectric force microscopy (DFM) has been previously developed to map charge carrier concentrations with nanometer-scale spatial resolution. However, it is challenging to quantitatively obtain the charge carrier concentration, since the dielectric force is also affected by the mobility. Here, we quantitative measured the charge carrier concentration at the saturation mobility regime via the rectification effect-dependent gating ratio of DFM. By measuring a series of n-type GaAs and GaN thin films with mobility in the saturation regime, we confirmed the decreased DFM-measured gating ratio with increasing electron concentration. Combined with numerical simulation to calibrate the tip–sample geometry-induced systematic error, the quantitative correlation between the DFM-measured gating ratio and the electron concentration has been established, where the extracted electron concentration presents high accuracy in the range of 4×10^{16} –1×10^{18} cm^{-3}. We expect the quantitative DFM to find broad applications in characterizing the charge carrier transport properties of various semiconducting materials and devices.

Keywords: dielectric force microscopy, charge carrier concentration, quantitative measurement, numerical simulation

PACS: 72.20.–I, 72.80.Ey, 68.37.Ps, 02.60.–x **DOI:** 10.1088/1674-1056/aca7e6

1. Introduction

The charge carrier concentration profile is one of the most important factors that determines the properties of semiconducting materials and performance of devices.[1–3] Conventional characterizations for charge carrier concentration, such as the field-effect transistor (FET), Hall effect and capacitance–voltage curve, have high accuracy but no spatial resolution. Scanning force microscopy (SFM) with nanometer-scale spatial resolution and various functional image modes has often been employed to investigate charge carrier concentration profiles.[4,5] For example, scanning microwave impedance microscopy and conducting atomic force microscopy measure the conductivity as the product of charge carrier concentration, elementary electron charge and mobility.[6,7] Scanning capacitance microscopy measures the tip–sample capacitance, which is also determined by the charge carrier concentration.[8] However, these contact imaging techniques rely on robust tip–sample contact, which suffers from delicate changes in tip radius, sample scratching, etc., during scanning.[9] Dielectric force microscopy (DFM), which is also known as the second harmonic signal of electrostatic force microscopy (EFM), is a noncontact SFM mode that measures the low-frequency dielectric force related to conductivity based on a microscopic Drude-level model; therefore, it can obtain the charge carrier concentration.[10–12]

DFM has been widely employed to investigate the charge carrier concentration profile in nanomaterials such as carbon nanotubes, organic thin films, perovskite thin films, inorganic metallic nanobeams and two-dimensional materials.[12–16] Metallic samples can be distinguished from semiconducting samples based on their distinct charge carrier concentration.[17] Using the inherited nanometer-scale spatial resolution, DFM can resolve the interface of metal–semiconductor junctions.[18,19] Furthermore, the accumulation or depletion of charge carriers can be tuned by applying a tip gate bias voltage (V_g), which is effective in identifying n-type, p-type and bipolar semiconducting samples.[20–24] In addition, the *in situ* measurement feature enables DFM to monitor the reversed polarity from p-type to n-type via the interfacial charge transfer process.[25,26] However, it is challenging to quantitatively extract the charge carrier concentration by DFM, where the dielectric force is also determined by another adjustable parameter, i.e., mobility.

In our previous work, a semi-logarithmic correlation between the gating ratio of DFM and the on/off ratio of FET was established, which confirms a significant rectification effect in-

†Corresponding author. E-mail: qchen2011@sinano.ac.cn
‡Corresponding author. E-mail: lwchen2018@sjtu.edu.cn

© 2023 Chinese Physical Society and IOP Publishing Ltd

duced by the gate bias voltage.[27] Here, we further demonstrated that the charge carrier concentration could be quantitatively extracted by using the charge carrier concentration-dependent rectification effect triggered by the tip gate bias voltage. By measuring a series of GaAs and GaN thin films with mobility in the saturation regime, the gating ratio of DFM was weakened by increasing the electron concentration, which is attributed to less significant rectification effect with higher electron concentration. Combined with numerical simulation to calibrate the tip–sample geometry induced systematic error, the correlation between the electron concentration and the gating ratio of DFM was quantitatively established, which presented high accuracy with the electron concentration of 4×10^{16}–1×10^{18} cm^{-3}.

2. Methods

2.1. Samples

The epitaxial growth of the GaAs and GaN thin films $\sim$ 1.5 μm respective on undoped GaAs substrates and sapphire substrates was performed with a Veeco GEN20A dual-chamber all-solid-state molecular beam epitaxy (MBE) equipped with a valved arsenic cracking cell. The typical growth rate of GaAs was 1 μm·h^{-1} with a V/III ratio of $\sim$ 30 at a growth temperature of 580 °C, where silicon was used as the n-type dopant. Typical growth rate of GaN was 0.5 μm·h^{-1} with the III/V ratio of $\sim$ 4.6 at growth temperature of 650 °C, where silicon was used as the n-type dopant. The material growth was described in detail in our previous work.[28]

2.2. Characterization

Hall effect measurements were performed on an HL 5500 PC Hall system (Accent) with Van der Pauw method. Spots welded at the corners, marked as 1, 2, 3, 4, of GaAs and GaN thin films ($\sim$ 0.8 mm × 0.8 mm) acted as ohmic contacts. The electron concentration (n) and mobility (μ_n) of GaAs and GaN thin films are respectively listed in Tables S1 and S2 and were obtained using the following equations:

$$n=\frac{2}{R_{H13}+R_{H24}}=\frac{2B}{eW\left(\frac{V_{H24}}{I_{13}}+\frac{V_{H13}}{I_{24}}\right)}, \tag{1}$$

$$\mu_n=\frac{1}{en\rho}, \tag{2}$$

where R_{H13} and R_{H24} are the Hall coefficients; I_{13} and I_{24} are the currents; V_{H13} and V_{H24} are the Hall voltages, and 1, 3 and 2, 4 are two sets of diagonal points on the sample; B is the magnetic induction intensity; e is the elementary electron charge; W is the thickness of the thin film; and ρ is the resistivity of the thin film.

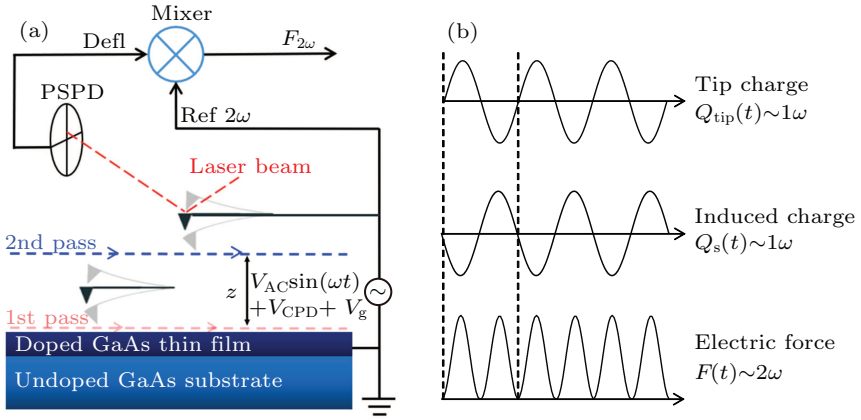


Fig. 1. (a) Schematic illustration of GaAs thin film sample measured by DFM. (b) Interaction between tip charge and induced charge on the sample.

DFM measurements were performed on a Cypher S AFM (Asylum Research, Oxford Instruments) in combination with an HF2LI lock-in amplifier (Zurich Instruments) using Cr/Au-coated conducting probes (NSC14, Mikromasch) with a spring constant (k) of $\sim$ 5 N·m^{-1} and a resonance frequency of $\sim$ 120 kHz. A double-pass scan mode was employed in DFM measurements, as shown in Fig. 1(a). In the first pass, standard AC mode was used to acquire the topography of the sample. In the second pass, the probe was lifted to a constant height ($\sim$ 10 nm) above the sample surface while an AC voltage ($V_{AC}\sin(\omega t)$, typically 2 V in amplitude and $\sim$ 60 kHz in frequency) was applied to the probe. The dielectric force $F_{2\omega}$ originating from the interaction between the oscillating tip charge and the induced charge of the sample ($\sim\sin(\omega t)$) became proportional to $\cos(2\omega t)$ as expressed below:

$$F_{2\omega}=\left(\frac{1}{2}f(\varepsilon,g)C+\frac{1}{4}\frac{\mathrm{d}C}{\mathrm{d}z}\right)V_{AC}^2, \tag{3}$$

where $f(\varepsilon,g)$ is the function of dielectric constant (ε) and geometric parameters (g), C is the capacitance of the tip–sample system, and $\mathrm{d}C/\mathrm{d}z$ is the corresponding capacitance gradient.[10] The force is demodulated at 2ω frequency as shown in Fig. 1(b).[29] By changing the tip gate bias voltage (V_g) from −4 V to 4 V, the charge carrier concentration of the

sample beneath the tip can be tuned to reflect the capacitance-dependent $F_{2\omega}$. The contact potential difference ($V_{\rm CPD}$) between the tip and the sample that interferes with $V_{\rm g}$ can be nullified by scanning Kelvin probe microscopy measurements (Table S3).

2.3. Simulation

The dielectric force $F_{2\omega}$ was obtained by numerically calculating the 2ω component of the electric force $F(t)$ between the tip and the sample via finite element analysis, as shown in Fig. 2. The calculation was performed using the Igor Pro 7.08 software. The tip was modeled as a truncated cone with a hemispherical apex. The height and half angle of the cone were set to 0.5 μm and 15°, respectively. The radius of the hemisphere was set to 30 nm. By applying tip bias $V(t) = V_{\rm AC}\sin(\omega t) + V_{\rm g}$, the tip charge $Q_{\rm tip}(t) = CV(t)$ was considered a point charge at the center of the hemisphere. The GaAs thin film was modeled as a rectangle with length ~ 1 μm and thickness ~ 100 nm, which was divided into 200×150 segments with length $\Delta x_i \sim 0.005$ μm and thickness $\Delta z_i \sim 0.667$ nm. The bottom edge of the GaAs thin film was grounded. $F(t)$ is the sum of the electric force between the tip charge and the sample charge of each segment,

$$F(t) = \frac{Q_{\rm tip}(t)}{4\pi\varepsilon_0}\sum_i \frac{z_i(n(x_i,z_i,t)-n)}{d_i^3}\Delta x_i \Delta z_i, \tag{4}$$

where (x_i, z_i) is the coordinate of the ith segment, $n(x_i, z_i, t)$ is the electron concentration of the ith segment of the sample, and $d_i = (x_i^2 + z_i^2)^{1/2}$ is the distance between the tip charge and the ith segment of the sample.

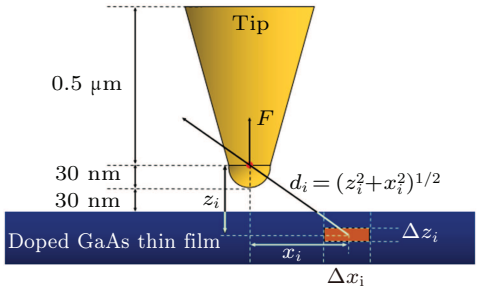


Fig. 2. Schematic illustration of the finite element numerical model of the tip–sample interaction in the DFM measurement.

To obtain the electron concentration profiles of the sample at different $V_{\rm g}$ and time t, the following Poisson's equation and continuity equation were simultaneously solved:

$$\nabla^2\varphi(x,z,t) = \frac{Q_{\rm tip}(t)+e(n(x,z,t)-n)}{\varepsilon_{\rm r}\varepsilon_0}, \tag{5}$$

$$\frac{\partial n(x,z,t)}{\partial t} = D_{\rm n}\nabla^2 n(x,z,t) - \mu_{\rm n}\nabla(n(x,z,t)\nabla\varphi(x,z,t)), \tag{6}$$

where $\varphi(x,z,t)$ is the potential distribution, $\varepsilon_{\rm r}$ is the relative dielectric constant of the air gap (~ 1) or GaAs (~ 12.9), ε_0 is the vacuum dielectric constant, $D_{\rm n} \sim 221$ cm$^2\cdot$s^{-1} is the diffusion coefficient of electrons, and $\mu_{\rm n} \sim 8500$ cm$^2\cdot$V$^{-1}\cdot$s^{-1} is the mobility of electrons.

The in-phase ($F_{\rm i}$) and quadrature ($F_{\rm q}$) parts of the 2ω component of $F(t)$ were calculated using

$$F_{\rm i} = \frac{2}{T}\int_0^T F(t)\cos(2\omega t)\,{\rm d}t, \tag{7}$$

$$F_{\rm q} = \frac{2}{T}\int_0^T F(t)\sin(2\omega t)\,{\rm d}t, \tag{8}$$

where $T = 1/\omega$ is the period of $V(t)$. The magnitude of the 2ω component ($F_{2\omega}$) of $F(t)$ was obtained from

$$F_{2\omega} = \sqrt{F_{\rm i}^2 + F_{\rm q}^2}. \tag{9}$$

3. Results and discussion

3.1. DFM measurements on GaAs thin films

Figures 3(a) and 3(c) are topography images of GaAs I ($n \sim 6.72\times10^{17}$ cm^{-3}) and GaAs II ($n \sim 2.89\times10^{18}$ cm^{-3}) thin films. The roughness of GaAs I and GaAs II thin films was ~ 0.8 nm and ~ 0.7 nm, respectively. Figures 3(b) and 3(d) are DFM images of both GaAs thin films at $V_{\rm g}$ from −4 V to 4 V. For GaAs I, the contrast in the DFM image at $V_{\rm g}$ between +4 V and 0 V was larger than that at $V_{\rm g}$ between −4 V and 0 V. For GaAs II, the contrast in the DFM image at $V_{\rm g}$ between +4 V and 0 V was close to that at $V_{\rm g}$ between −4 V and 0 V but smaller than that of GaAs I at $V_{\rm g}$ between +4 V and

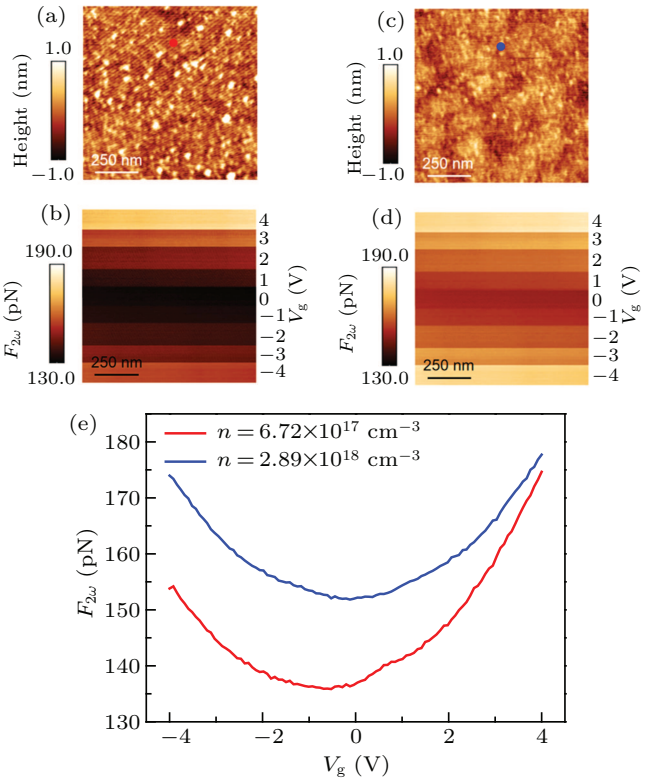


Fig. 3. (a)–(d) Topography and $F_{2\omega}$ images of GaAs thin films with (a), (b) $n = 6.72\times10^{17}$ cm^{-3} (GaAs I) and (c), (d) $n = 2.89\times10^{18}$ cm^{-3} (GaAs II), respectively. (e) $F_{2\omega}$ vs. $V_{\rm g}$ curves measured at the red point of GaAs I in (a) and the blue point of GaAs II in (c).

0 V. The contrast in the DFM image was quantitatively investigated by collecting dielectric force $F_{2\omega}$ vs. V_g curves of both GaAs thin films at the marked points in Figs. 3(a) and 3(c), as shown in Fig. 3(e), which showed little difference at other points (Fig. S1). The $F_{2\omega}$ of GaAs I and GaAs II thin films increased with both $+V_g$ and $-V_g$, which has also been reported in other materials such as organic thin films, carbon nanotubes and two-dimensional materials.[13,19,30] For GaAs I, the difference in $F_{2\omega}$ at V_g between +4 V and 0 V was $\sim$ 37.8 pN, which was larger than that at V_g between −4 V and 0 V ($\sim$ 17.0 pN). For GaAs II, the differences in $F_{2\omega}$ at V_g between +4 V and 0 V and between −4 V and 0 V were $\sim$ 25.6 pN and $\sim$ 21.9 pN, respectively, which were smaller than that of GaAs I at V_g between +4 V and 0 V.

The change in dielectric force $F_{2\omega}$ with V_g is attributed to rectification of electrons, i.e., accumulation at $+V_g$ and depletion at $-V_g$ beneath the tip. Figure 4(a) shows the electron concentration n profiles of the GaAs I and GaAs II thin films at V_g values of −4 V, 0 V and +4 V by numerical calculation via finite element analysis. The magnitude of n of GaAs I can be more efficiently modulated by V_g than that of GaAs II, i.e., which indicates a weakened rectification effect with a higher electron concentration. The n beneath the tip apex (at a distance of 0 μm) vs. V_g curves of GaAs I and GaAs II is plotted in Fig. 4(b) as an example, where n exhibited a more significant change with V_g than that at other sites. Based on the change in n profiles with V_g, $F_{2\omega}$ vs. V_g curves of GaAs I and GaAs II were calculated in Fig. 4(c) as detailed in Section 2. The calculated $F_{2\omega}$ of GaAs I and GaAs II increased with $+V_g$. Additionally, the difference in $F_{2\omega}$ of GaAs I at V_g between +4 V and 0 V was larger than both differences in $F_{2\omega}$ at V_g between +4 V and 0 V and between −4 V and 0 V of GaAs II. These results are consistent with the DFM measurement results in Fig. 3(e). However, the calculated $F_{2\omega}$ of GaAs I and GaAs II decreased with $-V_g$, which was the opposite of the DFM measurements.

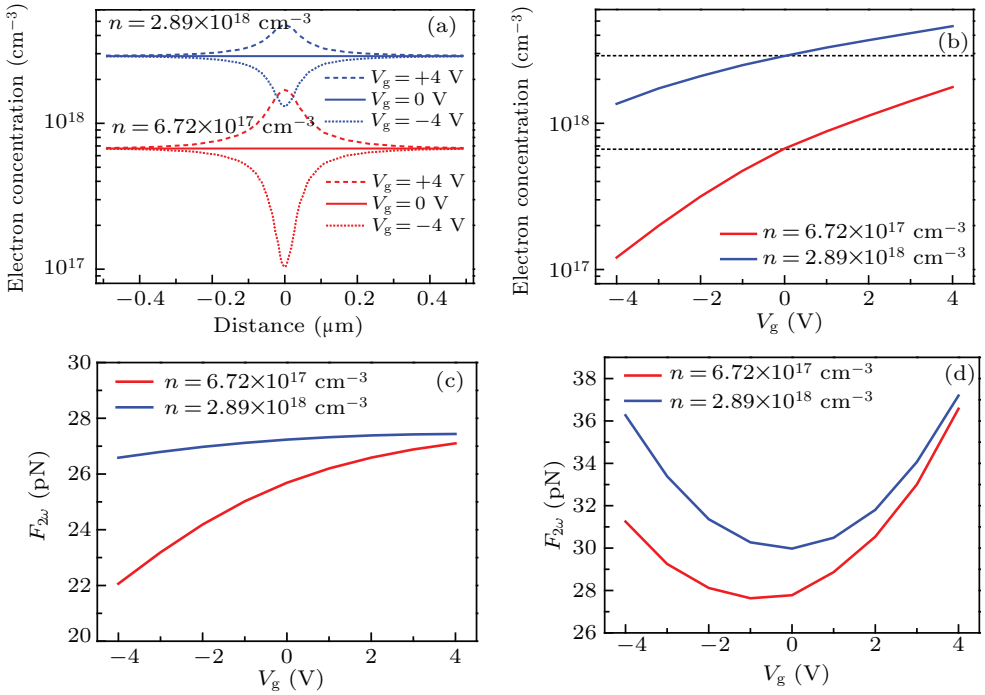


Fig. 4. (a) Simulated electron concentration profiles of GaAs thin films with $n = 6.72 \times 10^{17}$ cm^{-3} (red) and $n = 2.89 \times 10^{18}$ cm^{-3} (blue) at $V_g = +4$ V, 0 V and −4 V. (b) Corresponding electron concentration beneath the tip vs. V_g derived from (a). (c) Simulated $F_{2\omega}$ vs. V_g curves of GaAs thin films with $n = 6.72 \times 10^{17}$ cm^{-3} (red) and 2.89×10^{18} cm^{-3} (blue) under a constant tip–sample distance z. (d) Simulated $F_{2\omega}$ vs. V_g curves of GaAs thin films with $n = 6.72 \times 10^{17}$ cm^{-3} (red) and 2.89×10^{18} cm^{-3} (blue) under V_g-dependent z.

The contradiction in $F_{2\omega}$ vs. V_g between measurement and simulation is attributed to the V_g-dependent tip–sample distance z, which is not considered in the numerical calculation in Fig. 4(c). The reduction of z (δz) is determined by the DC component (F_{DC}) of the electric force divided by the probe spring constant k as expressed below:[31,32]

$$\delta z = \frac{F_{DC}}{k} = \frac{1}{2k}\frac{dC}{dz}\left(V_g^2 + \frac{1}{2}V_{AC}^2\right). \tag{10}$$

The δz shows a quadratic dependence on V_g, that is to say z decreases with the increasing absolute value of V_g, leading to increasing in $F_{2\omega}$ ($\delta F_{2\omega}$). Figure S2 shows $F_{2\omega}$ vs. V_g curves of an insulating SiO_2 sample, where $F_{2\omega}$ increases with the absolute value of V_g due to a smaller z even without any change in carrier concentration beneath the tip. For the GaAs thin film, the carrier concentration beneath the tip is also modulated by V_g, which tunes F_{DC} due to varied dC/dz. As a result, the change in δz will further tune the carrier concentration beneath the tip in turn. This complex interplay between V_g and

δz can be solved based on repeated iteration of Zeno's paradox as detailed in note S1 and Fig. S3. Figure 4(d) is the $F_{2\omega}$ vs. V_g curves calculated by numerical simulation after adding V_g-dependent δz. The calculated $F_{2\omega}$ of GaAs I and GaAs II increased with both $+V_g$ and $-V_g$, which is consistent with the DFM measurements in Fig. 3(e).

3.2. Quantitative extraction of the carrier concentration

The change in the $F_{2\omega}$ vs. V_g curves with n can be used to quantitatively extract the electron concentration of GaAs thin films, but it is also necessary to eliminate the interference of the change in the tip–sample distance. Although calculated $\delta z(+V_g)$ is slightly larger than $\delta z(-V_g)$, the ratio of the difference between $\delta F_{2\omega}(+V_g)$ and $\delta F_{2\omega}(-V_g)$ to $\delta F_{2\omega}(+V_g)$ is less than $\sim 4\%$ (Fig. 4(d)). In general, by extracting $\Delta F_{2\omega} = F_{2\omega}(+V_g) - F_{2\omega}(-V_g)$ vs. $\Delta V_g = +V_g - (-V_g)$ curves, the change in $F_{2\omega}$ induced by the difference between $\delta z(+V_g)$ and $\delta z(-V_g)$ can be basically eliminated. Figure 5(a) shows $\Delta F_{2\omega}$ vs. ΔV_g curves, where the gating ratio can be obtained from the slope of the linear fitting curve. The gating ratio of GaAs I ~ 2.416 pN·V^{-1} was larger than that of GaAs II ~ 0.452 pN·V^{-1} as shown in Fig. 5(b).

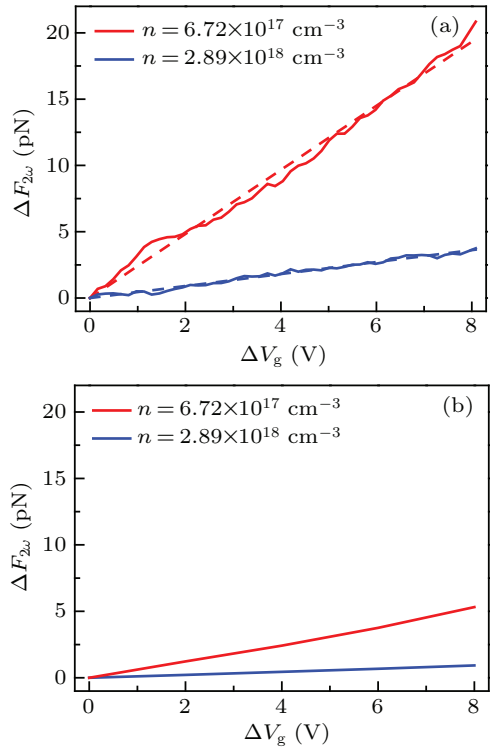


Fig. 5. (a) $\Delta F_{2\omega} = F_{2\omega}(+V_g) - F_{2\omega}(-V_g)$ vs. $\Delta V_g = V_g - (-V_g)$ curves of GaAs thin films with $n = 6.72 \times 10^{17}$ cm^{-3} (red) and 2.89×10^{18} cm^{-3} (blue) derived from DFM-measured $F_{2\omega}$ vs. V_g curves in Fig. 3(e). The dashed lines are linear fitting curves. (b) $\Delta F_{2\omega}$ vs. ΔV_g curves of GaAs thin films with $n = 6.72 \times 10^{17}$ cm^{-3} (red) and 2.89×10^{18} cm^{-3} (blue) derived from simulated $F_{2\omega}$ vs. V_g curves in Fig. 4(d).

The $\Delta F_{2\omega}$ linearly increases with ΔV_g, which is related to the concentration change of electron accumulation and depletion at $+V_g$ and $-V_g$, i.e., $\Delta n(V_g) = n(V_g) - n$. By extracting simulated n profiles at V_g from -4 V to $+4$ V and deducting the n profiles at $V_g = 0$ V, we obtained the corresponding Δn profiles at different V_g, as shown in Fig. S4. The $F_{2\omega}$ vs. V_g curves were calculated considering the change in z, from which the $\Delta F_{2\omega}$ vs. ΔV_g curves were extracted (Figs. 4(d) and 5(b)). Simulation results confirm the linear correlation between $\Delta F_{2\omega}$ and ΔV_g, where simulated gating ratio of GaAs I ~ 0.644 pN·V^{-1} was also larger than that of GaAs II ~ 0.114 pN·V^{-1}.

By measuring a series of GaAs thin films with n of 1.64×10^{17}–4.89×10^{18} cm^{-3} (Fig. S5), the gating ratio against n is plotted in Fig. 6(a). The measured gating ratio was much higher than the numerically calculated value. Nevertheless, the calculated gating ratio curves can overlap with those by DFM measurements after multiplying by a scaling factor $(\alpha) \sim 3.70$, which was obtained by minimizing the root-mean-square error (RMSE),

$$\mathrm{RMSE} = \sqrt{\sum_{i=1}^{P} w_r[i](\alpha G_{cal}[i] - G_{exp}[i])^2}, \tag{11}$$

where $P = 6$ is the number of GaAs thin films, $G_{cal}[i]$ is the calculated gating ratio of the ith sample, $G_{exp}[i]$ is the experimental measured gating ratio of the ith sample, and $w_r[i] = \frac{1}{G_{exp}[i]} \Big/ \sum_{i=1}^{P} \frac{1}{G_{exp}[i]}$ is the normalized weight ratio of the fitting error of the ith sample.

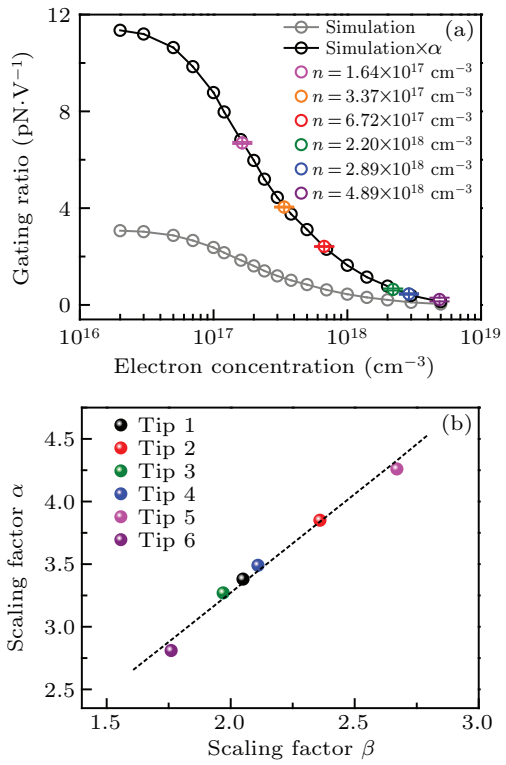


Fig. 6. (a) Calibrated gating ratio vs. n curves of GaAs thin films (black line with open circles) obtained from multiplying simulated curves (gray line with open circles) by scaling factor α based on DFM measurements (open circles). (b) Scaling factor α of gating ratio vs. scaling factor β of the tip–sample geometrical capacitance, in which the dash line is a linear fitting curve.

The gating ratio gradients are larger for n of 4×10^{16}–1×10^{18} cm^{-3} than those below 4×10^{16} cm^{-3} and above 1×10^{18} cm^{-3}. When n is less than 4×10^{16} cm^{-3}, inversion easily occurs at $-V_g$, since the Fermi level is near the middle of the band gap. In this case, holes accumulate at $-V_g$ and electrons accumulate at $+V_g$, which leads to a smaller difference in $F_{2\omega}$ at $-V_g$ and $+V_g$ and a smaller gating ratio gradient. For n above 1×10^{18} cm^{-3}, the modulation of n is not efficient by applying V_g, which leads to little difference in $F_{2\omega}$ and a small gating ratio gradient. Therefore, it is demonstrated that the electron concentration n extracted from the gating ratio vs. n curves shows high accuracy at 4×10^{16}–1×10^{18} cm^{-3}.

The scaling factor α is a key parameter for calibration of the charge carrier concentration. To investigate the factor that affects α, six tips were employed. Figure S6(a) shows calculated and measured gating ratio curves of these tips on a series of GaAs thin films with different n. The gating ratio curves via numerical calculation can overlap with those by measurements after multiplying by a scaling factor $\alpha \sim 3.38$, 3.85, 3.27, 3.49, 4.26 and 2.81 respectively. Considering that $F_{2\omega}$ and gating ratio are determined by the tip–sample geometrical capacitance, the $\mathrm{d}C/\mathrm{d}z$ curves of these tips at different tip–sample distance z were measured as shown in Fig. S6(b). The $\mathrm{d}C/\mathrm{d}z$ curves via numerical calculation can overlap with those by measurements after multiplying by a scaling factor $(\beta) \sim 2.05$, 2.36, 1.97, 2.11, 2.67 and 1.76, respectively. The scaling factor α against β is plotted in Fig. 6(b), in which a linear correlation can be established, indicating that there is indeed a relationship between α and the tip–sample geometrical capacitance gradient. Therefore, it shows significant difference in α from tip to tip even in one batch, indicating that α and the tip–sample geometrical capacitance of a series of tips are needed to be calibrated to build a database with two or more samples with different n. Then, α of other tips can be simply obtained based on their tip–sample geometrical capacitance.

3.3. Applicability of quantitative DFM

Here, the quantitative measurement of charge carrier concentration has been realized. Combined with experiments and simulations, the rectification effect correlated DFM-measured gating ratio weakens with increasing charge carrier concentration has been understood. To further calibrate the tip–sample geometry-induced systematic error, a universal quantitative correlation between n and the DFM-measured gating ratio has been established. To further corroborate the universal quantitative correlation, some n-type GaN thin films with mobility in the saturation regime have been employed, which exhibit n range from 1.57×10^{17} cm^{-3} to 3.46×10^{18} cm^{-3}. As shown in Fig. S7,the DFM-measured gating ratio is also quantitatively correlated to the n of GaN thin films by multiplying a scaling factor $\alpha \sim 3.55$.

As another adjustable parameter to determine $F_{2\omega}$, the charge carrier mobility may also influence the gating ratio. Nevertheless, the electron mobility μ_n does not change with V_g for various inorganic semiconducting materials, e.g., GaAs, GaN, etc., which reduces with higher doping concentration.[2] The n dependent μ_n may affect the dielectric force and the quantitative relationship between the DFM-measured gating ratio and n. Figure 7 is the numerical simulated $F_{2\omega}$ vs. μ_n curves for $n = 1\times10^{18}$ cm^{-3}, 1×10^{17} cm^{-3} and 1×10^{16} cm^{-3}, respectively. For $n = 1\times10^{18}$ cm^{-3}, $F_{2\omega}$ increases with μ_n and becomes saturated when it $> 10^{-4}$ cm^2·V^{-1}·s^{-1} (defined as the saturation mobility). While for $n = 1\times10^{18}$ cm^{-3}, 1×10^{17} cm^{-3} and 1×10^{16} cm^{-3}, the $F_{2\omega}$ becomes saturated when $\mu_n > 10^{-3}$ cm^2·V^{-1}·s^{-1} and 10^{-2} cm^2·V^{-1}·s^{-1}, respectively. Since the mobility of GaAs thin films $\sim 10^3$ cm^2·V^{-1}·s^{-1} and GaN thin films $\sim 10^2$ cm^2·V^{-1}·s^{-1} are both much larger than the saturation mobility, the effects of n dependent μ_n on $F_{2\omega}$ and the gating ratio independent of μ_n are not significant.

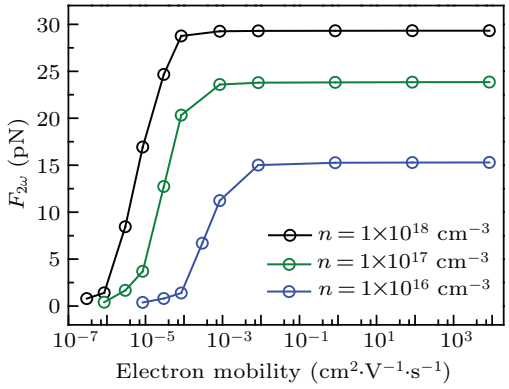


Fig. 7. Simulated $F_{2\omega}$ vs. μ_n curves at $V_g = 0$ V, where the black curve is at $n = 1\times10^{18}$ cm^{-3}, olive curve is at $n = 1\times10^{17}$ cm^{-3} and blue curve is at $n = 1\times10^{16}$ cm^{-3}.

4. Conclusion

In summary, the charge carrier concentration has been quantitatively measured using DFM by taking advantage of the rectification effect correlated with the gating ratio of DFM. For n-type GaAs and GaN thin films with mobility in the saturation regime, the rectification effect is strong when the electron concentration is moderate, and the gating ratio of DFM significantly decreases with increasing n. When the electron concentration is too low or too high, the rectification effect is weakened, and the change in DFM gating ratio with n is not remarkable. By calibrating the tip–sample geometry-induced systematic error via numerical simulation, the quantitative correlation between the electron concentration and the gating ratio of DFM was established, which presents high accuracy with electron concentrations of 4×10^{16}–1×10^{18} cm^{-3}. Quantitative DFM is expected to be widely used in various semiconducting materials and devices to provide important technical support in the study of charge carrier transport properties.

Acknowledgements

Project supported by the National Key R&D Program of China (Grant No. 2021YFA1202802), the National Natural Science Foundation of China (Grant Nos. 21875280, 21991150, 21991153, and 22022205), the CAS Project for Young Scientists in Basic Research (Grant No. YSBR-054), and the Special Foundation for Carbon Peak Neutralization Technology Innovation Program of Jiangsu Province, China (Grant No. BE2022026).

References

[1] Koster L J A, Smits E C P, Mihailetchi V D and Blom P W M 2005 *Phys. Rev. B* **72** 085205
[2] Sze S M and Ng K K 2006 *Physics of semiconductor devices* (New Jersey: John wiley & sons) pp. 16–75
[3] Li P, Ai X, Zhang Q H, Gu S J, Wang L J and Jiang W 2021 *Chin. Chem. Lett.* **32** 811
[4] Pingree L S C, Reid O G and Ginger D S 2009 *Adv. Mater.* **21** 19
[5] Chen X, Lai J Q, Shen Y B, Chen Q and Chen L W 2018 *Adv. Mater.* **30** 1802490
[6] Lai K, Kundhikanjana W, Kelly M and Shen Z X 2008 *Rev. Sci. Instrum.* **79** 063703
[7] Hussain S, Xu K Q, Ye S L, Lei L, Liu X M, Xu R, Xie L M and Cheng Z H 2019 *Front. Phys.* **14** 33401
[8] Barrett R C and Quate C F 1991 *J. Appl. Phys.* **70** 2725
[9] Linde F, Yadavalli N S and Santer S 2013 *Appl. Phys. Lett.* **103** 253101
[10] Cherniavskaya O, Chen L W, Weng V, Yuditsky L and Brus L E 2003 *J. Phys. Chem. B* **107** 1525
[11] Zhang J, Ye F Y, Chen Q, Lu W, Cai J H and Chen L W 2013 *Sci. Sin.: Chim.* **43** 1806
[12] Zhang J, Lu W, Li Y S, Cai J H and Chen L W 2015 *Acc. Chem. Res.* **48** 1788
[13] Jiang Y P, Qi Q, Wang R, Zhang J, Xue Q K, Wang C, Jiang C and Qiu X H 2011 *ACS Nano* **5** 6195
[14] Chen Q, Chen L, Ye F Y, Zhao T, Tang F, Rajagopal A, Jiang Z, Jiang S, Jen A K Y, Y. X, Cai J H and Chen L W 2017 *Nano Lett.* **17** 3231
[15] Li Z J, Wu J J, Hu Z P, Lin Y, Chen Q, Guo Y Q, Liu Y H, Zhao Y C, Peng J, Chu W S, Wu C Z and Xie Y 2017 *Nat. Commun.* **8** 15561
[16] Xu R, Ye S L, Xu K Q, Lei L, Hussain S, Zheng Z Y, Pang F, Xing S Y, Liu X M, Ji W and Cheng Z H 2018 *Nanotechnology* **29** 355701
[17] Lu W, Xiong Y, Hassanien A, Zhao W, Zheng M and Chen L W 2009 *Nano Lett.* **9** 1668
[18] Lu W, Xiong Y and Chen L W 2009 *J. Phys. Chem. C* **113** 10337
[19] Lu W, Zhang J, Li Y S, Chen Q, Wang X P, Hassanien A and Chen L W 2012 *J. Phys. Chem. C* **116** 7158
[20] Zhang K, Marzari N and Zhang Q 2013 *J. Phys. Chem. C* **117** 24570
[21] Zhang K, Wang X, Sun L, Zou J, Wang J, Liu Z, Chen T, Tay B K and Zhang Q 2017 *Appl. Phys. Lett.* **111** 043106
[22] Lei L, Xu R, Ye S L, Wang X S, Xu K Q, Hussain S, Li Y J, Sugawara Y, Xie L M, Ji W and Cheng Z H 2018 *J. Phys. Commun.* **2** 025013
[23] Kang Y B, Jeon D and Kim T 2020 *J. Phys. Chem. C* **124** 18316
[24] Jeon D, Kang Y and Kim T 2021 *ACS Appl. Electron. Mater.* **4** 124
[25] Zhang J, Lu W, Li Y S, Lu D, Zhang T, Wang X P and Chen L W 2012 *J. Phys. Chem. Lett.* **3** 3509
[26] Chen Q, Lu W, Wu Y K, Ding H Y, Wang B and Chen L W 2014 *Chin. J. Chem. Phys.* **27** 582
[27] Li Y S, Ge J, Cai J H, Zhang J, Lu W, Liu J and Chen L W 2014 *Nano Res.* **7** 1623
[28] Dai P, Ji L, Tan M, Uchida S, Wu Y Y, Abuduwayiti A, Heini M, Guo Q, Bian L F, Lu S L and Yang H 2017 *Sol. Energy Mater. Sol. Cells* **171** 118
[29] Lu W, Wang D and Chen L W 2007 *Nano Lett.* **7** 2729
[30] Park J, Jeon D, Kang Y B, Yu Y J and Kim T 2019 *J. Phys. Chem. Lett.* **10** 4010
[31] Qi G C, Yan H, Guan L, Yang Y L, Qiu X H, Wang C, Li Y B and Jiang Y P 2008 *J. Appl. Phys.* **103** 114311
[32] Qi G C, Yang Y L, Yan H, Guan L, Li Y B, Qiu X H and Wang C 2009 *J. Phys. Chem. C* **113** 204